Automated Alignment With Respect to a Moving Inductive Wireless Charger

Ivan Cortes and Won-Jong Kim, *Senior Member, IEEE*

***Abstract*— Wireless charging is an attractive technology that often promises increased mobility for electrical devices. However, commonly available wireless charging systems are generally intolerant to misalignment between the charger and the receiving device due to the need for inductive coupling between the two, defeating the promise of mobility. Many techniques have been studied to address this issue, including improved electrical circuits, novel charger coil designs, and the use of sensors for detecting misalignment. In this article, a new arrangement of sensing coils is used to detect lateral misalignment between a moving wireless charger and a mobile robot. Data from the sensing coils are used in a dual-loop control of the robot. The inner loop controls the robot velocities and consists of a linear quadratic regulator with integral action. The outer loop provides reference velocities to the inner loop based on the readings of the sensing coils. Using this method, an experimental mobile robot maintains alignment within 2 cm with respect to a 5-W wireless charger that moves up to 0.145 m/s. This automated alignment method is a low-cost solution that enables mobile systems, such as autonomous vehicles, to wirelessly charge while the charger is moving.**

***Index Terms*— Linear quadratic optimal control, mobile robot, sensing coils, wireless charging.**

I. Introduction

WIRELESS power transfer (WPT) has intrigued scientists and engineers for many decades [1], [2]. The appeals of WPT include a reduction of wires, elimination of exposed electrical contacts, increased device mobility, and reduced battery size. Such features immediately affect the safety and convenience of many consumer products. This widespread impact is exemplified by the recent marketing of wireless charging for mobile devices and electric vehicles [3], [4].

Commercial wireless chargers operate using inductive power transfer (IPT) technology. In this method, the charger and the receiving device each contain a coil. When placed near each other, the coils in the charger and the receiving device are closely coupled and the energy is transferred via magnetic induction. However, any misalignment between the coils significantly reduces the inductive coupling, decreasing the effective power transfer. For this reason, wireless charging systems are generally intolerant to misalignment [5], [6].

Manuscript received October 29, 2020; revised January 27, 2021; accepted February 28, 2021. Date of publication March 9, 2021; date of current version March 22, 2022. *(Corresponding author: Ivan Cortes.)*

The authors are with the Department of Mechanical Engineering, Texas A&M University, College Station, TX 77843-3123 USA (e-mail: icorteso@tamu.edu; wjkim@tamu.edu).

Digital Object Identifier 10.1109/TTE.2021.3064782

Many studies investigated solutions for misalignment intolerance in IPT systems. One approach is to strengthen the inductive link between the charger and the receiver over a larger range of misalignments. This has been accomplished by improving the electrical circuits, introducing additional coils, or modifying coil geometries [7]–[10]. Another approach is to detect and correct misalignment at the time of WPT. Methods for detecting misalignment include the use of cameras, auxiliary coils, phase-detection circuits, or conventional sensors [11]–[15].

Studies of wireless charging typically consider static applications, where a stationary charger transfers power to a device that is not moving. However, some mobile systems—such as electric vehicles, water vessels, or robots—could benefit from wireless charging while they move [16]–[19]. Misalignment issues are complicated in such cases due to the movement dynamics of the mobile systems. Thus, solutions for misalignment reduction in moving IPT scenarios have recently gained attention. Dynamic wireless charging for vehicles typically features stationary, in-ground chargers with novel coil geometries and optimized power strategies [16], [1]. Coil misalignment in these cases is often corrected by adjusting the vehicle steering in real-time [12]–[15]. Other studies have proposed mobile chargers as a cost-effective alternative to in-ground chargers [20], [21]. In this case, a mobile charging station is brought to the vehicle, and the vehicle must maintain alignment with the moving charger.

The solution presented in this article provides automated, lateral alignment between a device and a moving wireless charger. The misalignment is measured using a modified version of the sensing coils presented in [11] and [22]. In the previous work, the sensing coils were used in a static scenario only. This article extends the use of the sensing coils to dynamic wireless charging. As the wireless charger moves, the receiving device maintains proper alignment with the charger using real-time feedback from the sensing coils. A mobile robot, equipped with a wireless charging receiver, is used as a test vehicle. A wireless charger is moved in a predetermined path, and the robot's own movement is controlled to continuously position the robot above the charger. This solution is easily scaled for implementation in other mobile systems, such as electric vehicles, to enable more mobility during wireless charging.

This article consists of seven sections. Section II describes a conceptual scenario for mobile robot wireless charging that is the focus of this article. In Section III, the proposed misalignment-sensing coils and their operation are presented.

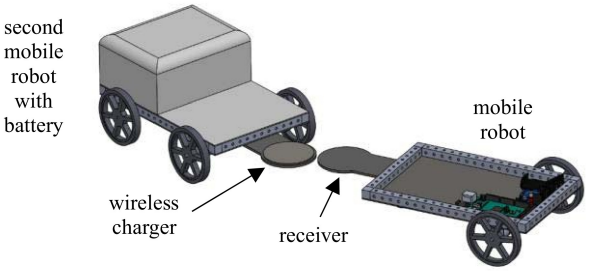

Fig. 1. Example scenario of wireless charging with a moving charger. One mobile robot has a wireless charger, and the other robot has a receiver.

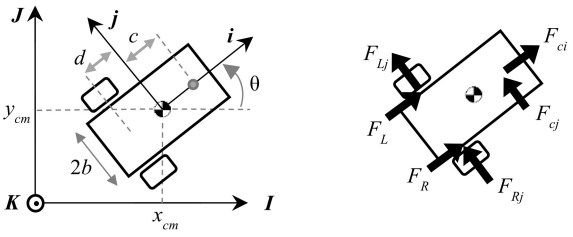

Fig. 2. Differential-drive mobile robot with global and body-fixed frames.

The controller design for the robot is detailed in Section IV. The experimental hardware, including a mobile robot and charger-positioning mechanisms, is described in Section V. The experimental measurements of the mobile robot positioning above the moving wireless charger are presented in Section VI. Finally, Section VII offers the conclusions of this article.

II. Wireless Charging With a Moving Charger

Consider the wireless charging scenario depicted in Fig. 1. A mobile robot is equipped with a wireless charging receiver. Rather than returning to a charging station, a wireless charger is brought to the mobile robot using a second mobile robot with a large battery. For effective power transfer, the receiver must continuously be aligned with the charger. If properly controlled, the charger and the mobile robot can move together, enabling the robot to perform its primary function while it charges. The challenge is continuously sensing and correcting any misalignment between the charger and the receiver as they move. This article details one solution that enables automated alignment using inexpensive sensing coils and a dual-loop control scheme.

The scenario described in Fig. 1 is representative of other systems where the charger and the receiver move laterally with respect to one another. One example is wireless charging for electric vehicles. Another example is water vessels that move up and down due to waves. In this case, the charger and the receiver are mounted vertically, as in [18], so that they remain approximately parallel as the vessel moves.

The mobile robot in this article serves as a test system for the misalignment-sensing coils and control strategy. Mobile robots are commonly used in the literature to approximate larger vehicles [23], [24]. However, the forthcoming experiment is a low-speed application on a flat surface. In this case, vibrations or other high-frequency disturbances are not a factor. Previous work investigated wireless charging for fast-moving systems, especially electric vehicles [25]–[27].

A. Differential-Drive Mobile Robot

In this article, a differential-drive mobile robot with two dc-motor-driven wheels and one caster roller is considered. Fig. 2 depicts the mobile robot from a top view and establishes two coordinate frames along with some dimensions. The global inertial frame is defined by the basis $\{\boldsymbol{I}, \boldsymbol{J}, \boldsymbol{K}\}$ and the robot body-fixed frame by the basis $\{\boldsymbol{i}, \boldsymbol{j}, \boldsymbol{k}\}$. The $\boldsymbol{k}$-axis passes through the robot center of mass, and the $\boldsymbol{i}$-axis is aligned with the robot's axis of symmetry, forming the angle θ with respect to $\boldsymbol{I}$. The wheelbase center is at $-d\boldsymbol{i}$, and the ball caster is at $c\boldsymbol{i}$.

The two main forces acting on the robot, F_{L} and F_{R}, are due to rolling without slipping of the left and right wheels, respectively. With a motor armature resistance R, torque constant K_{t}, back electromotive force (EMF) constant K_{b}, and negligible inductance, the force from each wheel on the robot is

$$F = \frac{K_{\mathrm{t}}}{Rr}V - \frac{J}{r}\ddot{\phi} - \left(\frac{B}{r} + \frac{K_{\mathrm{t}}K_{\mathrm{b}}}{Rr}\right)\dot{\phi} \tag{1}$$

where V is the motor input voltage, J is the rotational inertia, and B is the viscous damping coefficient. The wheel has radius r and its angular position is ϕ. Other forces acting on the robot are the lateral wheel forces, $F_{\mathrm{L}j}$ and $F_{\mathrm{R}j}$, and the caster friction forces, F_{ci} and F_{cj}. The inclusion of the dc motor characteristics is an improvement over the previous modeling in [22].

Rolling without slipping of the wheels results in the well-known nonholonomic constraints

$$v_i = \frac{r}{2}\left(\dot{\phi}_{\mathrm{R}} + \dot{\phi}_{\mathrm{L}}\right) \tag{2}$$

$$\omega = \dot{\theta} = \frac{r}{2b}\left(\dot{\phi}_{\mathrm{R}} - \dot{\phi}_{\mathrm{L}}\right) \tag{3}$$

which give the robot $\boldsymbol{i}$ velocity and angular velocity in terms of the wheel velocities. With no lateral slip of the wheels, $F_{\mathrm{L}j}$ and $F_{\mathrm{R}j}$ are eliminated from the equations of motion, and the $\boldsymbol{j}$ acceleration of the mass center is simply

$$a_j = \ddot{\theta}d. \tag{4}$$

The $\boldsymbol{i}$ acceleration of the mass center is

$$a_i = a_{\mathrm{wb}i} - \omega^2 d \tag{5}$$

where $a_{\mathrm{wb}i}$ is the wheelbase $\boldsymbol{i}$ acceleration, obtained by taking the time derivative of (2). Using (1)–(5), the robot equations of motion are found to be

$$\begin{aligned} a_i = &-\left(\frac{2(K_{\mathrm{t}}K_{\mathrm{b}} + BR) + CRr^2}{mRr^2 + 2JR}\right)v_i - \left(\frac{2JRd}{mRr^2 + 2JR}\right)\omega^2 \\ &+ \left(\frac{K_{\mathrm{t}}r}{mRr^2 + 2JR}\right)V_{\mathrm{R}} + \left(\frac{K_{\mathrm{t}}r}{mRr^2 + 2JR}\right)V_{\mathrm{L}} \end{aligned} \tag{6}$$

$$\ddot{\theta} = -\left(\frac{2b^2(K_{\mathrm{t}}K_{\mathrm{b}} + BR) + CRr^2(c+d)^2}{Rr^2\left(I_{\mathrm{cm}} + md^2\right) + 2JRb^2}\right)\omega$$

TABLE I
MOBILE ROBOT PARAMETERS

Parameter	Measured or Calculated Value
m	0.976 kg
I_{cm}	0.01 kg·m^2
b	0.1 m
r	0.04 m
c	0.15 m
d	0.06 m
C	1.0 N·s/m
K_t	0.3739 N·m/A
K_b	0.7801 V·s/rad
R	9 Ω
J	0.002 kg·m^2
B	0.001913 N·m·s/rad

$$+\left(\frac{K_t br}{Rr^2\left(I_{\rm cm}+md^2\right)+2JRb^2}\right)V_{\rm R} -\left(\frac{K_t br}{Rr^2\left(I_{\rm cm}+md^2\right)+2JRb^2}\right)V_{\rm L} \quad (7)$$

where m is the robot mass, $I_{\rm cm}$ is the moment of inertia about the center of mass, and C is a viscous damping coefficient for the caster friction force.

For small angular velocities, the ω^2 term in (6) is approximately 0. The resulting linear system is simplified and can be expressed in the state-space form

$$\dot{\boldsymbol{x}}=\begin{bmatrix}-\alpha & 0\\ 0 & -\beta\end{bmatrix}\boldsymbol{x}+\begin{bmatrix}\gamma & \gamma\\ \varepsilon & -\varepsilon\end{bmatrix}\boldsymbol{u},\quad \boldsymbol{y}=\begin{bmatrix}1 & 0\\ 0 & 1\end{bmatrix}\boldsymbol{x} \quad (8)$$

where

$$\boldsymbol{x}=[v_i \quad \omega]^{\rm T},\quad \boldsymbol{u}=[V_{\rm R} \quad V_{\rm L}]^{\rm T}$$

and the symbols in (8) are defined in (6) and (7). This system is observable and controllable. Table I lists the robot parameter values used in the forthcoming experiments. These values were found by direct measurement and experimentation.

The differential-drive mobile robot considered here offers simple dynamics for controller design. Forthcoming controller analysis should be repeated if using a different mobile system, such as a four-wheel-drive vehicle. Suitable models for such vehicles are common in the literature. Many vehicles share some characteristics with the mobile robot used here, such as nonholonomic behavior or movements adequately described by the linear and angular velocities.

III. 2-D MISALIGNMENT-SENSING COILS

The working principle for the proposed misalignment-sensing coils is reviewed in this section. A sensing coil is a loop of wire that experiences an induced voltage when exposed to a time-varying magnetic field. The induced voltage serves as a measurement of the magnetic flux. The misalignment-sensing coils in this article are an arrangement of eight circular wire loops that are used to estimate the misalignment magnitude and direction for a wireless charging system. A similar concept was used in previous work for IPT systems [11], [14], [15].

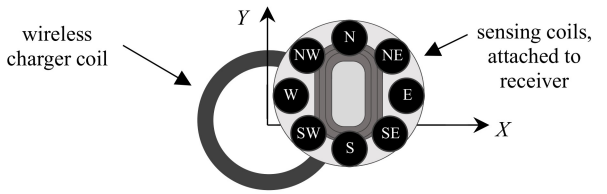

Fig. 3. Configuration of the eight misalignment-sensing coils (top view).

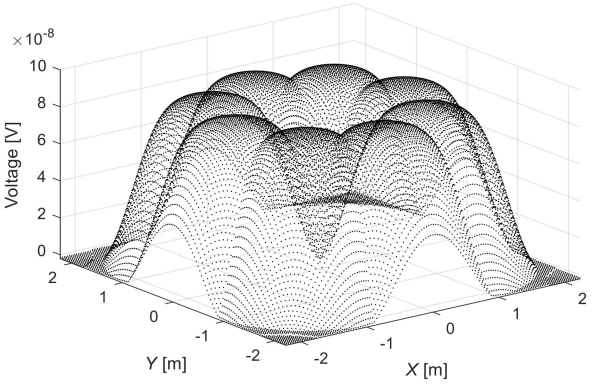

Fig. 4. Simulated induced voltage for eight sensing coils as a function of lateral position above a circular wireless charger with a radius of 1 m.

An IPT wireless charger is a source of alternating magnetic field. For a circular charging coil, the magnetic flux density is axisymmetric and largest directly above the coil. A secondary coil will experience the greatest induced voltage when it is in the area directly above the charger. Thus, power transfer is most effective when the receiver is concentric with the charger.

A. Voltage Trend of Eight Sensing Coils

Consider the arrangement of eight sensing coils depicted in Fig. 3. The sensing coils are fixed to the receiver in a circular pattern and are labeled using cardinal directions. The east direction aligns with the positive x- axis. The wireless charger is fixed at the origin, and the sensing coils move with the receiver on the xy plane at a fixed Z height. The sensing coils have one-fourth the radius of the charger coil and are arranged so they form a circle slightly larger than the charger.

Fig. 4 shows the simulated induced voltage magnitudes of the eight sensing coils as a function of the receiver position. The simulation was generated in MATLAB by applying the Biot–Savart law and Faraday's law for magnetic induction, with 0.25-m-radius sensing coils at the 0.5-m height from the charger. The charger coil has 1-m radius and a 1-A sinusoidal current at 1 rad/s frequency. Each hill in Fig. 4 is the voltage increase for one of the eight coils when that coil is concentric with the charger. When the receiver is aligned with the charger, all sensing coils experience near-zero induced voltage, and any disturbance from this position increases the voltage in at least one sensing coil. This behavior is a result of the sensing coil placement described in Fig. 3. To reproduce this behavior in a general system, the coils should be arranged in a circle slightly larger than the wireless charger coil. The dimensions of the coils are selected to give a favorable induced voltage range

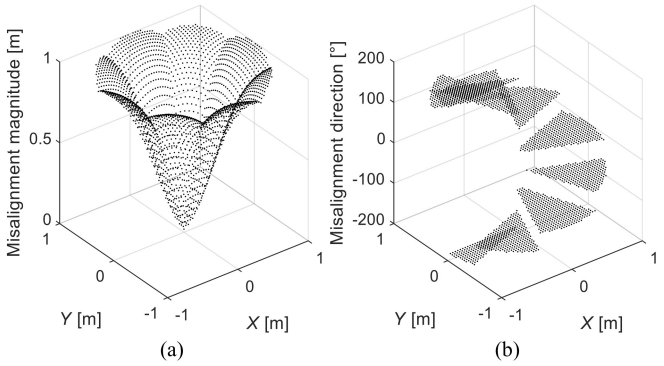

Fig. 5. (a) Misalignment magnitude and (b) direction estimates using the proposed misalignment-sensing coils.

when they are above the charger. This voltage range can be found by simulation or experimentation, but Faraday's law of magnetic induction dictates that the induced voltage increases with coil size and number of loops [11], [13].

B. Misalignment Detection Using Eight Sensing Coils

Suppose the receiver is disturbed from the aligned position. The proposed use of the eight misalignment-sensing coils is as follows. First, the induced voltage magnitude of each coil is recorded. Then, the sensing coil with the largest voltage magnitude indicates the dominant misalignment direction. Finally, the misalignment magnitude is estimated using the largest voltage along with an equation that is fit to the voltage trend. This procedure is different from the approach in [11] and [22], which relied on the voltage difference between two coils.

Fig. 5 shows sample results if the eight sensing coils are used as suggested. A linear equation is used to convert the sensor voltages from Fig. 4 to a misalignment magnitude. The linear coefficient is such that the peak voltage gives a misalignment magnitude of 1 m. To ensure the magnitude equation is a one-to-one function, the range of misalignments is limited to a 1-m radius from the origin. The misalignment direction estimate is the angle for the cardinal direction of the dominant sensing coil.

The true misalignment magnitude would appear as a unit cone in Fig. 5(a), and the true misalignment direction as a smooth surface from $-180°$ to $180°$ in Fig. 5(b). The estimates have some errors but allow for an informed, corrective action for small misalignments. Additional sensing coils or a nonlinear magnitude calculation would make the estimates closer to the ideal values. Increased accuracy from using more sensing coils would come at a modest cost increase. One suggestion for the optimal number of coils is the minimum number that enables satisfactory misalignment detection for the desired application. If the movement of the charger is slow, or the corrective action of the moving device is fast, then the eight-coil configuration is sufficient for sensing and correcting any lateral misalignment up to one charger coil radius. If a larger range or a better resolution of misalignment direction is needed, more sensing coils are added. One practical limitation for adding more coils is that they may overlap each other.

IV. Controller Design

A dual-loop controller is used for the position control of the mobile robot, as proposed in [22]. The block diagram for the controller is shown in Fig. 6. The inner loop uses state feedback to control the robot velocities, and the outer loop uses classical control to provide reference velocities to the inner loop based on the measured position error of the robot.

The dual-loop structure is versatile and common in mobile systems. It provides an advantage over single-loop controllers because multiple sensors are incorporated. Velocity feedback in the inner loop is provided by wheel encoders. The inner loop is a velocity-tracking system that is blind to the global robot position. The position measurement is made in the outer loop by the sensing coils.

A. Inner Loop Controller

The inner loop controller ensures that the mobile robot tracks the reference velocities, v_{ir} and ω_r. To this end, a linear quadratic regulator (LQR) with integral action is implemented, as shown in Fig. 7. The integrator in the loop enables tracking of a reference input and provides some robustness to parameter uncertainties in the robot model.

Let an augmented state vector be defined as

$$\boldsymbol{x}_a = \begin{bmatrix} v_i & \omega & \int v_{ie}dt & \int \omega_e dt \end{bmatrix}^{\mathrm{T}}. \tag{9}$$

A quadratic cost function is defined as

$$J = \int_0^\infty \left(\boldsymbol{x}_a^{\mathrm{T}}\boldsymbol{Q}\boldsymbol{x}_a + \boldsymbol{u}^{\mathrm{T}}\boldsymbol{R}\boldsymbol{u} + 2\boldsymbol{x}_a^{\mathrm{T}}\boldsymbol{N}\boldsymbol{u}\right)dt. \tag{10}$$

It is well-known that the feedback gain matrix, $\boldsymbol{K}$ in Fig. 7, that minimizes (10) is found by solving a Riccati equation containing the weight matrices $\boldsymbol{Q}$, $\boldsymbol{R}$, and $\boldsymbol{N}$. One must select the values in these matrices so that $\boldsymbol{x}_a$ and $\boldsymbol{u}$ are penalized according to the control objectives.

Suppose the robot accelerations are to be penalized in the cost, J. The accelerations are expressed in the quadratic form

$$\dot{\boldsymbol{x}}^{\mathrm{T}}\dot{\boldsymbol{x}} = \boldsymbol{x}^{\mathrm{T}}\boldsymbol{A}^{\mathrm{T}}\boldsymbol{A}\boldsymbol{x} + \boldsymbol{u}^{\mathrm{T}}\boldsymbol{B}^{\mathrm{T}}\boldsymbol{B}\boldsymbol{u} + 2\boldsymbol{x}^{\mathrm{T}}\boldsymbol{A}^{\mathrm{T}}\boldsymbol{B}\boldsymbol{u} \tag{11}$$

where $\boldsymbol{A}$ and $\boldsymbol{B}$ are the state and input matrices from (8), respectively. Comparing (11) with (10), the weight matrices are selected as

$$\mathbf{Q} = \left[\begin{array}{c|cc} \boldsymbol{A}^{\mathrm{T}}\boldsymbol{A} & \boldsymbol{O}_{2\times 2} & \\ \hline \boldsymbol{O}_{2\times 2} & w_{\mathrm{v}} & 0 \\ & 0 & w_\omega \end{array}\right] \boldsymbol{R} = \boldsymbol{B}^{\mathrm{T}}\boldsymbol{B} \quad \boldsymbol{N} = \left[\begin{array}{c} \boldsymbol{A}^{\mathrm{T}}\boldsymbol{B} \\ \hline \boldsymbol{O}_{2\times 2} \end{array}\right] \tag{12}$$

where $\boldsymbol{O}_{2\times 2}$ is a 2×2 zero matrix. With these weight matrices, the cost (10) includes the robot accelerations and the augmented error integral states. The augmented states are weighted by the scalar values w_{v} and w_ω. For the mobile robot in this article, the weights were selected by simulation iterations to achieve an inner loop rise time of about 0.2 s for both robot states. The resulting optimal feedback gain matrix is

$$\boldsymbol{K} = \left[\begin{array}{c|c} \boldsymbol{K}_x & \boldsymbol{K}_e \end{array}\right] = \left[\begin{array}{cc|cc} 21 & 2 & -529 & -59 \\ 21 & -2 & -529 & 59 \end{array}\right]. \tag{13}$$

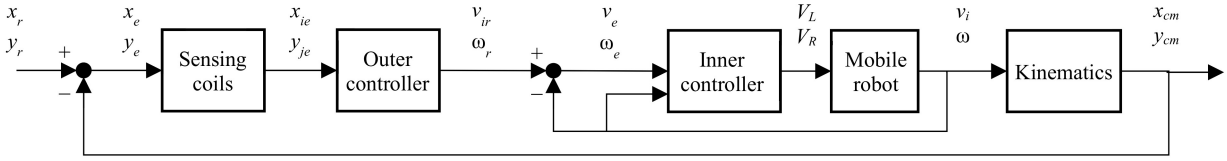

Fig. 6. Dual-loop controller for the mobile robot. The outer loop provides the inner loop with robot reference velocities based on the position error of the IPT receiver with respect to the moving charger. The inner loop tracks the reference velocities.

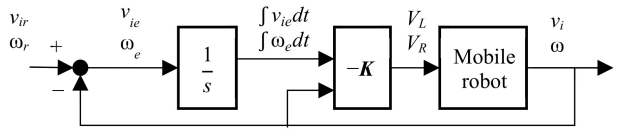

Fig. 7. Mobile robot's inner control loop with an LQR, featuring integral action. This controller enables the robot to track reference velocities.

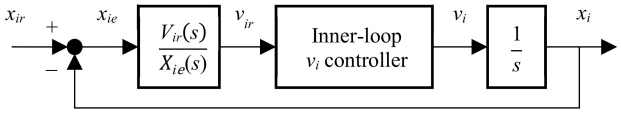

Fig. 8. Equivalent system for a pure distance error that would result in a straight motion.

Each column in $\boldsymbol{K}$ indicates how much a respective state in (9) contributes to the motor input voltages. In particular, note that a velocity error is weighted more than the other states—reflecting the high cost of a linear velocity error. There is also symmetry between the two rows of $\boldsymbol{K}$. The linear velocity states affect both the motor voltages equally, whereas the angular velocity states affect the motor voltages with an opposite sign. This result is consistent with the differential-drive mobile robot dynamics. One can use this knowledge to further tune the weights in (12) or to evaluate $\boldsymbol{K}$ directly. The final selection of $\boldsymbol{K}$ was supported by experiments with our physical robot.

With a $\boldsymbol{K}$ of the form in (13), the inner loop becomes dynamically decoupled. The equivalent inner loop system is

$$\dot{\boldsymbol{x}}_a = \left[\begin{array}{c|c} \boldsymbol{A}-\boldsymbol{B}\boldsymbol{K}_{\mathrm{x}} & -\boldsymbol{B}\boldsymbol{K}_{\mathrm{e}} \\ \hline -\boldsymbol{I}_{2\times 2} & \boldsymbol{O}_{2\times 2} \end{array}\right]\boldsymbol{x}_{\mathrm{a}} + \left[\begin{array}{c} \boldsymbol{O}_{2\times 2} \\ \hline \boldsymbol{I}_{2\times 2} \end{array}\right]\begin{bmatrix} v_{\mathrm{ir}} \\ \omega_r \end{bmatrix} \quad (14)$$

where $\boldsymbol{I}_{2\times 2}$ is the 2×2 identity matrix. The transfer function of this system, using the same output as (8), is

$$\mathbf{T}(s) = -\left[s^2\boldsymbol{I}_{2\times 2} - s(\boldsymbol{A}-\boldsymbol{B}\boldsymbol{K}_{\mathrm{x}}) - \boldsymbol{B}\boldsymbol{K}_{\mathrm{e}}\right]^{-1}\boldsymbol{B}\boldsymbol{K}_{\mathrm{e}}. \quad (15)$$

With $\boldsymbol{K}$ of the form in (13), every matrix in (15) is diagonal. Then, $\boldsymbol{T}(s)$ is also diagonal, and the inner loop is dynamically decoupled. This result, along with the single integrator in the LQR, means the inner loop will behave like two independent Type-I systems, one for v_i and the other for ω.

B. Outer Loop Controller

The outer loop controller provides reference velocities to the inner loop based on the position error of the robot. Since the reference velocities are in the robot body-fixed frame, the outer loop should have some knowledge about the robot pose. This is naturally accomplished if the outer loop sensor is attached to the robot itself. Then, the sensor observes the target position in the robot frame of reference.

The proposed misalignment-sensing coils are attached to the mobile robot and provide a measurement of the robot position error with respect to the wireless charger. With the arrangement described in Section III, the sensing coils produce a 2-D error measurement in the $\boldsymbol{i}$–$\boldsymbol{j}$ directions of Fig. 2. Let the $\boldsymbol{i}$-direction error be $x_{i\mathrm{e}}$ and the $\boldsymbol{j}$-direction error $y_{j\mathrm{e}}$. Then, let the robot reference velocities be calculated by the outer loop controllers

$$\frac{V_{i\mathrm{r}}(s)}{X_{i\mathrm{e}}(s)} = 8 + \frac{1}{s} \quad (16)$$

$$\frac{\Omega_r(s)}{Y_{j\mathrm{e}}(s)} = 32 + \frac{4}{s}. \quad (17)$$

These controllers were designed by considering the cases with only distance and heading angle error, respectively. Both these cases linearize the outer loop kinematics and allow for design using classical methods. For example, considering a pure distance error is equivalent to considering the single-input single-output (SISO) system in Fig. 8, where only the $\boldsymbol{i}$ velocity is controlled and the robot moves in a straight line. Similarly, a pure heading angle error would result in a pure rotation motion. The pure rotation analysis is an approximation since the linearized system (8) is valid only for small ω.

The outer loop controller design followed a typical classical method, with the aid of root locus and simulated step responses of the system. Using (15), it is observed that the inner loop controller transfer function in Fig. 8 has no free integrators. Having an integrator in (16) makes the system Type II, resulting in zero steady-state error for ramp x_{ir} inputs. Zero error for ramp inputs is desired for the intended application of a moving wireless charger. Thus, a proportional–integral (PI) controller was used, and the gains were tuned with the aid of simulation. The same process was used for the ω_{r} controller. The selection criteria for the PI gains were to achieve stability, a rise time less than 1 s, and near-zero tracking error for a ramp input. Fig. 9 shows the simulated ramp responses for pure distance and pure heading angle errors using the PI gains in (16) and (17). The ramp inputs were scaled to give the maximum linear and angular velocities of the experimental robot. The velocity tracking errors approach 0, as desired.

C. Reference Velocity Limits

Not all reference velocities are attainable by the mobile robot due to motor saturation. Providing unreasonably large

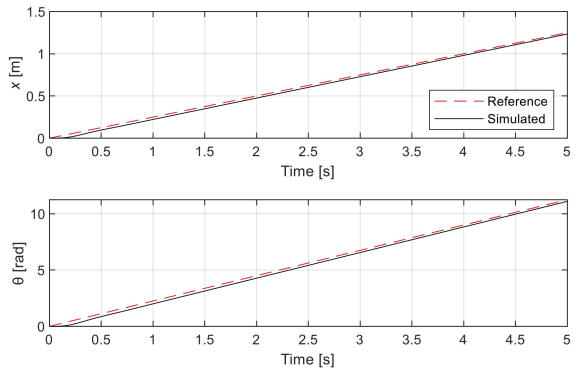

Fig. 9. Simulated ramp responses for pure distance error (top) and pure heading angle error (bottom) using the outer loop controllers (16)–(17).

reference velocities causes integrator windup to occur in the inner loop of Fig. 3, as the velocity error integrals continue to accumulate when the robot motors are at maximum speed. A scheme is formulated to limit the reference velocities produced by the outer loop controllers.

Let the maximum speed of each robot wheel be $\dot{\phi}_{\max}$. From (2) and (3), the maximum robot velocities are

$$v_{i,\max} = \frac{r}{2}\left(\dot{\phi}_{\max} + \dot{\phi}_{\max}\right) = r\dot{\phi}_{\max} \tag{18}$$

$$\omega_{\max} = \frac{r}{2b}\left(\dot{\phi}_{\max} - \left(-\dot{\phi}_{\max}\right)\right) = \frac{r}{b}\dot{\phi}_{\max}. \tag{19}$$

However, $v_{i,\max}$ and $\omega_{\max}$ cannot simultaneously be achieved. The maximum value of each can only occur when the other is 0. Obtaining a large v_i and ω is a competing objective. One way to address this is to limit either v_{ir} or ω_r when the other is large.

Suppose the angular velocity control is prioritized so that the heading angle error is eliminated before the distance error. The following limiting scheme is implemented for v_{ir} and ω_r:

$$|\omega_r| \leq \frac{r}{b}\dot{\phi}_{\max} \tag{20}$$

$$|v_{ir}| \leq r\dot{\phi}_{\max} - b|\omega_r|. \tag{21}$$

In (20), the magnitude of ω_r is limited to $\omega_{\max}$. In (21), the magnitude of v_{ir} is limited to a value dependent on ω_r. As ω_r increases to $\omega_{\max}$ the upper limit of v_{ir} becomes zero. Only when ω_r is zero will v_{ir} be allowed to reach $v_{i,\max}$. Thus, ω_r is allowed its full range, but v_r is limited by the current ω_r. Using this limiting scheme, only achievable reference velocities are given to the inner loop and the angular velocity tracking is prioritized.

V. Experimental Setup

A. Differential-Drive Mobile Robot

The differential-drive mobile robot pictured in Fig. 10 was constructed to test the sensing coils and control strategy. The physical dimensions and other characteristics of the mobile robot are listed in Table I.

The two robot wheels are driven by two 12-V dc motors with 100:1 gear ratio (Pololu product #3490) and are equipped with encoders that provide 1000 counts per wheel revolution. The encoder readings and controller calculations are performed by an Arduino Mega 2560 microcontroller board at a sampling period of 30 ms. The motors are driven using an L298N motor driver with pulsewidth modulation (PWM) signals generated by the Arduino. Eight AA batteries in series power the robot, allowing for maximum linear and angular velocities of about 0.5 m/s and 4.5 rad/s, respectively.

The robot is also equipped with a sensing coil assembly at the front of the chassis, near the ball caster. The sensing coil construction is detailed in Section V-C.

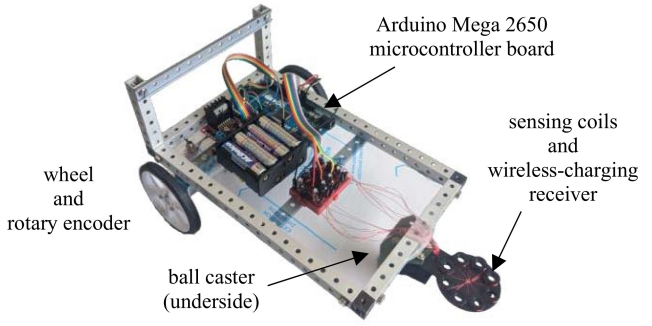

Fig. 10. Experimental differential-drive mobile robot with wheel encoders and the proposed misalignment-sensing coils. The robot chassis is 16 cm wide and 25 cm long.

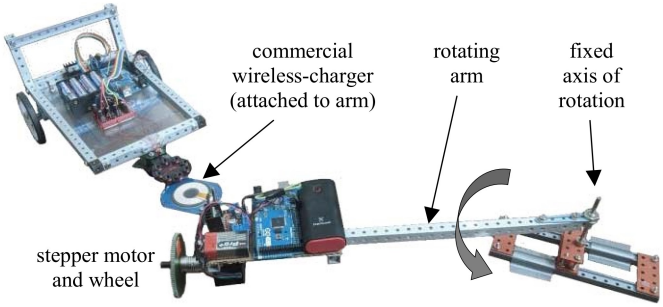

Fig. 11. First charger positioning mechanism: a rotating arm with a stepper-motor-driven wheel. The mobile robot moves independent of the rotating arm. The arm is about 50 cm long.

B. Charger Positioning Mechanisms

To move the wireless charger in a controlled manner, a rotating arm mechanism was used, as pictured in Fig. 11. The rigid arm rotates about a fixed axis and is actuated by a bipolar stepper motor (model 17HS13-0404S) connected to a wheel. Again, an Arduino Mega 2560 is used to control the stepper motor via an L298N motor driver and 9-V battery. By controlling the step frequency of the motor, the speed and position of the arm are known at all times.

The wireless charger is attached rigidly to the end of the rotating arm, so the charger moves in a circle of 51-cm radius, at constant height, and parallel to the ground. The mobile robot attempts to follow the charger using measurements from the sensing coils and the controller detailed in Section IV. During every trial, the position of the charger and mobile robot is recorded, allowing for plotting of the results.

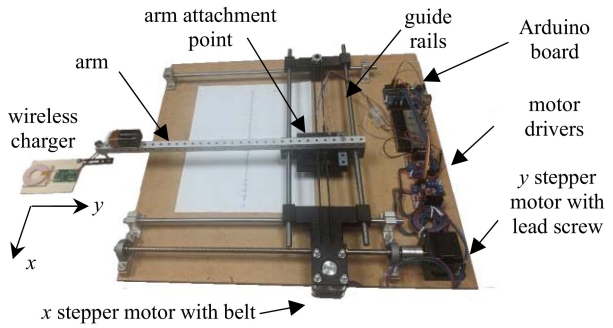

Fig. 12. Second charger positioning mechanism: a 2-D Cartesian positioner actuated by two stepper motors. The wireless charger, attached to the end of the arm, can move within an area of about 25 cm × 25 cm.

The rotating arm replaces the second mobile robot in Fig. 1. While the arm does not provide all the possible motions of a mobile robot, it provides a 2-D motion that is easily controlled and recorded using a single actuator. Furthermore, a circular motion offers the technical challenge of tracking higher order polynomials, rather than simple step or ramp inputs. Successful tracking of the circular motion demonstrates that the robot is capable of tracking a variety of other movements.

A second mechanism, pictured in Fig. 12, was used to test linear patterns of charger movement with sudden turns. Two stepper motors actuate the movement in the x- and y-directions. The same arm from Fig. 11 was attached to this second mechanism. This setup allows for the charger to be moved within an area about 25 cm × 25 cm at a constant height. The pattern of movement was controlled using an Arduino board, with positioning resolutions of 0.2 and 0.042 mm in the x- and y-directions, respectively. The speed of the movement is controlled by changing the time delay between motor steps.

C. Wireless Charger and Misalignment-Sensing Coils

The wireless charger used was the Yootech T500PB, a 5-W mobile-phone charger that uses the Qi wireless charging standard. The compatible receiver used was the Adafruit Qi receiver (product #1901). The receiver is attached to the front of the mobile robot, along with the sensing coil assembly. For maximum power transfer, the receiver must be concentric with the wireless charger. When aligned, the receiver is at the height of 2 mm from the charger. The actual power transfer from the charger to the receiver was not measured for this article. Previous works studied the power transfer for such systems, especially in the presence of misalignments [6].

To create the sensing coil assembly, a custom fixture was 3-D-printed. Each coil was wound in the fixture with 15 turns of AWG 25 enamel-coated copper wire. As illustrated in Fig. 3, the sensing coils have one-fourth the radius of the wireless charger and are spaced so that they form a circle slightly larger than the charger. In addition to the coil assembly, a diode half-bridge rectifier with a smoothing capacitor and shunt resistor was implemented separately for each coil. This circuit converts the ac voltage of each coil to a dc value. The capacitor and resistor values used were 10 μF and 1 kΩ to achieve a sensor response faster than the controller sampling period of 30 ms. At each control loop iteration, the dc voltage of the eight sensing coils is read by the Arduino board with 5-mV resolution.

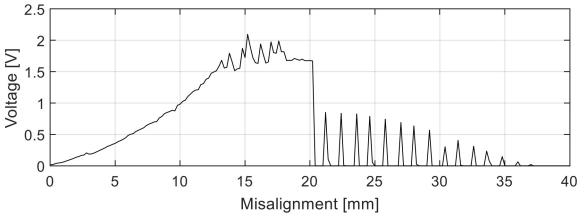

Fig. 13. Measured sensing coil voltage as the sensing coil assembly moves from the aligned position to the direction opposite the sensing coil.

When the receiver is concentric with the charger, the sensing coils experience a negligible voltage. Any disturbance from this position results in the voltage increase for one or more of the sensing coils. As proposed in Section II, the largest voltage among the sensing coils is used to estimate the misalignment magnitude and direction. Fig. 13 shows the measured voltage of the W coil as the receiver is moved from the aligned position to the E-direction, as referenced in Fig. 3. Beyond the 20-mm misalignment, the receiver goes out of range and the charger enters a low-power pulsating mode. Except for this behavior, the voltage trend agrees with the simulation of Fig. 4. From 0 to 15 mm, the misalignment magnitude is approximately

$$\delta = 0.01\ V_{\text{meas}} \tag{22}$$

where V_{meas} is the measured voltage in volts and δ is the misalignment magnitude in meters. This approximation was used for the charger–receiver experiment in this article. Any deviation from this setup, such as a change in the distance between the charger and receiver, will alter the coil voltages. Therefore, external factors such as uneven terrain or significant vibrations would lead to inaccurate estimation of misalignment amount. The experiment in this article was performed on flat ground and in a controlled environment.

Once the direction and magnitude of the misalignment are estimated with respect to the receiver, the position error of the mobile robot is calculated using trivial geometry. For example, let the N coil be aligned with the robot $\boldsymbol{i}$-axis and the W coil be aligned with the $\boldsymbol{j}$-axis. Then, a voltage in the N coil indicates that $x_{ie} \approx \delta$. As another example, a voltage in the NW coil indicates that $x_{ie} \approx (\sqrt{2}/2)\delta$ and $y_{ie} \approx (\sqrt{2}/2)\delta$.

VI. Experimental Results

Experiments were conducted to test the misalignment-sensing coils and mobile robot alignment with respect to the moving wireless charger. The velocity tracking performance of the inner control loop of Fig. 6 was also investigated.

A. Charger Tracking

To test the automated alignment with respect to a moving wireless charger, the mobile robot and rotating arm mechanism were first placed in a starting position such that the receiver was aligned with the charger. At this instant, the charger was located at the global origin and the robot faced the positive

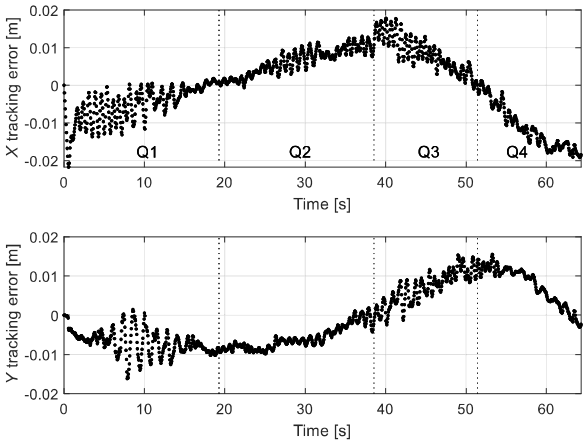

Fig. 14. Tracking error of the robot-mounted receiver with respect to the moving wireless charger. The charger trajectory is a circle, as shown in Fig. 15, and the vertical lines mark the four quadrants of the circle.

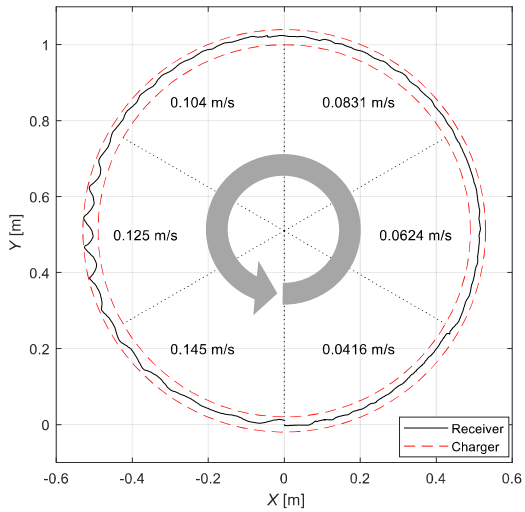

Fig. 15. Experimental results for the automated alignment of the mobile robot with respect to the moving wireless charger. The charger and robot-mounted receiver both start at the origin and then move counterclockwise. At each multiple of 60°, the movement speed is increased, giving a final tangential speed of 0.145 m/s. The receiver remains within the bounds of the charger, which is marked by the dashed lines.

x-direction. Then, the rotating arm mechanism was activated so that the charger moved in a counterclockwise circle with a 51-cm radius. The positions of the wireless charger and receiver were recorded as the arm rotated and the mobile robot followed. Several trials were run to test various movement speeds.

In the first trial, the charger moved at 0.0815 rad/s, or a tangential speed of 0.0416 m/s. This is about one-tenth the maximum linear speed of the mobile robot. Once the charger completed a half-circle of movement, the speed of the arm was increased by 50%. The Cartesian tracking errors for this trial are plotted in Fig. 14. These results indicate a lag behavior in the tracking response. During the first quadrant of the circular motion, from 0 to 19 s, the receiver lags the charger, resulting in negative X- and Y-tracking errors. In the second quadrant, from 19 to 38 s, the X movement of the charger reverses direction and the X-tracking error becomes positive, while the Y error remains negative. A comparable trend is seen in the last two quadrants of the movement. Despite the increased movement speed for the last two quadrants, the tracking error in both the directions remains under 2 cm. This is significant because a larger position error would risk deactivation of the wireless charger, as seen in Fig. 13.

A second trial was performed to test larger movement speeds. Fig. 15 presents the X–Y plot of this trial, where the position of the receiver is shown as a solid line and the edges of the moving charger are shown as dashed lines. As in the first experimental trial, the receiver tracks within 2 cm of the charger center, keeping the wireless charger active. The charger movement is increased at each 60° of the circle movement, giving the final tangential speed of 0.145 m/s. At higher speeds, oscillatory behavior of the charger movement is more prominent. Nevertheless, the robot performs corrective action to bring the receiver close to alignment with the charger.

A circular movement of the wireless charger is a challenging tracking task for any mobile system, since a circular trajectory, in theory, contains infinite polynomial components. The controller developed in Section IV was tuned for ramp input tracking. Thus, the tracking error recorded in the experiment trials was not surprising, and the tracking error increases with movement velocity. If the mobile robot does not react quickly enough to misalignment, the sensing coils will be too far from the charger to detect the movement. The goal of control, which was achieved in the two presented trials, was to keep the tracking error within the area of the wireless charger so that it would continue to function properly.

A third trail was performed using the second positioning mechanism pictured in Fig. 12. Unlike the circular trajectory of Fig. 15, this trial features sharp corners as the charger changes direction. Fig. 16 shows the motion of the charger and robot-mounted receiver during the trial. Once again, the receiver follows the charger movement closely, with an error less than 2 cm. The small zig-zag patterns in the receiver trajectory are attributed to friction and gear play in the robot wheels. Such behavior was more prominent in this trial because the charger trajectory caused the robot to move backward or turn in place as it tracked the charger. There is also some noticeable overshoot in the top left corner of the motion. Nevertheless, the receiver remains within alignment from start to finish.

The robot control was effective despite the approximations made in using the sensing coils. The sensing coils only provide an estimate of the misalignment direction as one of the eight directions, and the misalignment magnitude is approximated using a linear equation. Fig. 13 suggests that as long as the misalignment magnitude is less than 2 cm, one sensing coil will experience an induced voltage and the control action will bring the system closer to alignment. This is the behavior seen in Fig. 15, despite some small oscillations. Thus, the sensor arrangement is suitable for applications where the path to alignment is not critical, and it is more important for the receiver to remain within a certain area above the charger. If the starting position of the robot was slightly disturbed, the initial movement of the robot would be more drastic,

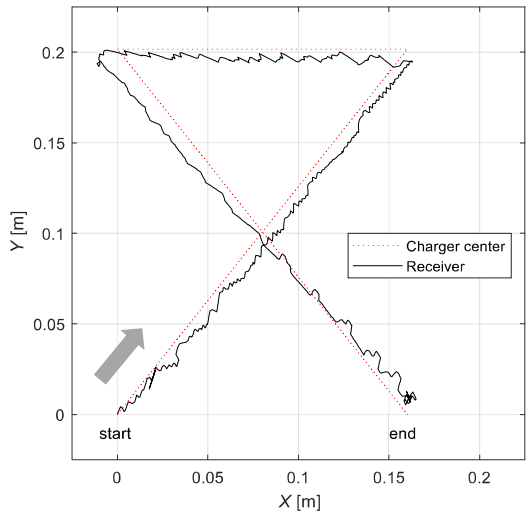

Fig. 16. Experimental results for the automated alignment of the mobile robot with respect to the moving wireless charger. In this trial, the charger moves in a cross pattern at a maximum speed of 0.02 m/s. The robot-mounted receiver follows the charger movement with less than 2 cm of error.

but the remainder of the trial would be similar to what was presented.

Importantly, every mobile system has a finite response time, so there is a maximum speed that can be tracked if the system starts from rest. If the sensing coils ever exit the area above the charger, tracking the charger movement is likely to fail. The maximum allowable speed for alignment is dependent on the dynamics of the vehicle, especially considering the response time of the inner control loop and velocity limits. At worst, the solution presented in this article is a useful addition to the existing vehicle guidance systems that improves charging alignment in the presence of small disturbances. At best, the sensing coils are used as the primary sensor to couple a vehicle with a moving wireless charger. The experiment in this article is an example of the latter, with the limitation of a slow movement speed.

B. Inner Control Loop Velocity Tracking

One of the advantages of the dual-loop structure is the ability to tune the velocity tracking response in the inner loop independently of the position measurements in the outer loop. Fig. 17 shows the reference and measured velocities of the mobile robot for an experimental reference velocity profile.

From 0 to 4 s, the $\boldsymbol{i}$ velocity of the robot tracks a ramp input. There is a small dead band until about 0.5 s, which is due to motor starting friction. Other than this behavior, the robot velocity tracks the ramp input with a minor initial overshoot and near-zero steady-state error.

From 4 to 6 s, the $\boldsymbol{i}$ reference velocity steps down by half, and the robot tracks this step with an overshoot of about 50%. However, the response time is fast, and the near-zero steady-state error is reached in about 1.5 s.

Starting at 6 s, the reference angular velocity ramps up until it reaches the maximum robot angular velocity at about 8 s. The measured angular velocity tracks the ramp input with a small error. Furthermore, the rise in angular velocity

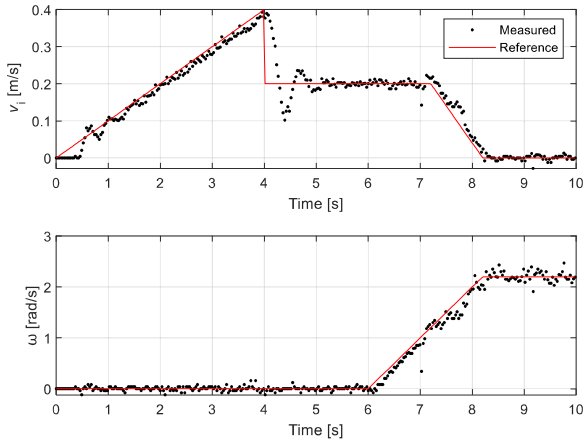

Fig. 17. Effectiveness of the robot inner control loop is demonstrated by plotting the measured robot velocities along with an experimental reference velocity profile.

response does not noticeably affect the measured $\boldsymbol{i}$ velocity, demonstrating the dynamic decoupling of the robot system.

From about 7 to 10 s, the reference velocity saturation scheme discussed in Section IV-C is demonstrated. First, the increasing reference angular velocity causes the $\boldsymbol{i}$ reference velocity to decrease. As the angular velocity reaches its maximum, the reference $\boldsymbol{i}$ velocity becomes 0. This limiting scheme ensures that only achievable velocities are input to the inner loop. Otherwise, integrator windup would occur.

VII. Conclusion

This article demonstrates the use of misalignment-sensing coils and a dual-loop controller to achieve automated alignment with respect to a moving wireless charger. In the proposed configuration, eight sensing coils are used to detect lateral misalignment between a circular charging coil and a receiver that is parallel to the charger. The sensing coils provide an estimate of misalignment direction and magnitude as long as one or more of the sensing coils remains in the region above the charger. For the mobile robot tested, an LQR inner loop and PI outer loop were sufficient for dynamic tracking of a moving charger, and the robot-mounted receiver remained closely aligned with the moving charger at low speeds. This proof of concept provides the foundation for similar applications in larger mobile systems. The number of sensing coils may be increased, at low cost, to improve the sensing resolution, but their working principle will remain unchanged. The control strategy should be adjusted for the intended mobile system, but a dual-loop structure provides the advantage of speed control in the inner loop using the system's usual speed sensors. The sensing coils offer an effective way to close the outer loop and allow for following the movement of the wireless charger.

References

[1] H. Feng, R. Tavakoli, O. C. Onar, and Z. Pantic, "Advances in high-power wireless charging systems: Overview and design considerations," *IEEE Trans. Transport. Electrific.*, vol. 6, no. 3, pp. 886–919, Sep. 2020.

[2] G. A. Covic and J. T. Boys, "Inductive power transfer," *Proc. IEEE*, vol. 101, no. 6, pp. 1276–1289, Jun. 2013.

[3] S. Y. Hui, "Planar wireless charging technology for portable electronic products and Qi," *Proc. IEEE*, vol. 101, no. 6, pp. 1290–1301, Jun. 2013.
[4] R. W. Carlson and B. Normann, "Test results of the PLUGLESS inductive charging system from Evatran group, inc," *SAE Int. J. Alternative Powertrains*, vol. 3, no. 1, pp. 64–71, Apr. 2014.
[5] I. Mayordomo, T. Drager, P. Spies, J. Bernhard, and A. Pflaum, "An overview of technical challenges and advances of inductive wireless power transmission," *Proc. IEEE*, vol. 101, no. 6, pp. 1302–1311, Jun. 2013.
[6] Y. Gao, A. Ginart, K. B. Farley, and Z. T. H. Tse, "Misalignment effect on efficiency of wireless power transfer for electric vehicles," in *Proc. IEEE Appl. Power Electron. Conf. Expo. (APEC)*, Los Angeles, CA, USA, Mar. 2016, pp. 3526–3528.
[7] Z. Dang, Y. Cao, and J. A. A. Qahouq, "Reconfigurable magnetic resonance-coupled wireless power transfer system," *IEEE Trans. Power Electron.*, vol. 30, no. 11, pp. 6057–6069, Nov. 2015.
[8] T. Duong and J.-W. Lee, "A dynamically adaptable impedance-matching system for midrange wireless power transfer with misalignment," *Energies*, vol. 8, no. 8, pp. 7593–7617, Jul. 2015.
[9] J. P. W. Chow, N. Chen, H. S. H. Chung, and L. L. H. Chan, "An investigation into the use of orthogonal winding in loosely coupled link for improving power transfer efficiency under coil misalignment," *IEEE Trans. Power Electron.*, vol. 30, no. 10, pp. 5632–5649, Oct. 2015.
[10] L. Zhao, D. J. Thrimawithana, and U. K. Madawala, "Hybrid bidirectional wireless EV charging system tolerant to pad misalignment," *IEEE Trans. Ind. Electron.*, vol. 64, no. 9, pp. 7079–7086, Sep. 2017.
[11] I. Cortes and W.-J. Kim, "Lateral position error reduction using misalignment-sensing coils in inductive power transfer systems," *IEEE/ASME Trans. Mechatronics*, vol. 23, no. 2, pp. 875–882, Apr. 2018.
[12] K. Hwang *et al.*, "An autonomous coil alignment system for the dynamic wireless charging of electric vehicles to minimize lateral misalignment," *Energies*, vol. 10, no. 3, pp. 1–20, Mar. 2017.
[13] Y. Gao, C. Duan, A. A. Oliveira, A. Ginart, K. B. Farley, and Z. T. H. Tse, "3-D coil positioning based on magnetic sensing for wireless EV charging," *IEEE Trans. Transport. Electrific.*, vol. 3, no. 3, pp. 578–588, Sep. 2017.
[14] Y. Gao, A. A. Oliveira, K. B. Farley, and Z. T. H. Tse, "Magnetic alignment detection using existing charging facility in wireless EV chargers," *J. Sensors*, vol. 2016, pp. 1–9, Jan. 2016.
[15] X. Liu, C. Liu, W. Han, and P. W. T. Pong, "Design and implementation of a multi-purpose TMR sensor matrix for wireless electric vehicle charging," *IEEE Sensors J.*, vol. 19, no. 5, pp. 1683–1692, Mar. 2019.
[16] D. Patil, M. K. McDonough, J. M. Miller, B. Fahimi, and P. T. Balsara, "Wireless power transfer for vehicular applications: Overview and challenges," *IEEE Trans. Transport. Electrific.*, vol. 4, no. 1, pp. 3–37, Mar. 2018.
[17] M. Chabalko, J. Besnoff, M. Laifenfeld, and D. S. Ricketts, "Resonantly coupled wireless power transfer for non-stationary loads with application in automotive environments," *IEEE Trans. Ind. Electron.*, vol. 64, no. 1, pp. 91–103, Jan. 2017.
[18] G. Guidi, J. A. Suul, F. Jenset, and I. Sorfonn, "Wireless charging for ships: high-power inductive charging for battery electric and plug-in hybrid vessels," *IEEE Electrific. Mag.*, vol. 5, no. 3, pp. 22–32, Sep. 2017.
[19] A. Hajiaghajani, D. Kim, A. Abdolali, and S. Ahn, "Patterned magnetic fields for remote steering and wireless powering to a swimming microrobot," *IEEE/ASME Trans. Mechatronics*, vol. 25, no. 1, pp. 207–216, Feb. 2020.
[20] E. A. ElGhanam, M. S. Hassan, and A. H. Osman, "Deployment optimization of dynamic wireless electric vehicle charging systems: A review," in *Proc. IEEE Int. IoT, Electron. Mechatronics Conf.*, Vancouver, BC, Canada, Sep. 2020, pp. 1–7.
[21] D. Kosmanos *et al.*, "Route optimization of electric vehicles based on dynamic wireless charging," *IEEE Access*, vol. 6, pp. 42551–42565, Jul. 2018.
[22] I. Cortes and W.-J. Kim, "Autonomous positioning of a mobile robot for wireless charging using computer vision and misalignment-sensing coils," in *Proc. Annu. Amer. Control Conf. (ACC)*, Milwaukee, WI, USA, Jun. 2018, pp. 4324–4329.
[23] E. Kayacan, "Closed-loop error learning control for uncertain nonlinear systems with experimental validation on a mobile robot," *IEEE/ASME Trans. Mechatronics*, vol. 24, no. 5, pp. 2397–2405, Oct. 2019.
[24] X. Liang, H. Wang, Y.-H. Liu, Z. Liu, and W. Chen, "Leader-following formation control of nonholonomic mobile robots with velocity observers," *IEEE/ASME Trans. Mechatronics*, vol. 25, no. 4, pp. 1747–1755, Aug. 2020.
[25] N. Wang, Q. Yang, M. Xue, and J. Guo, "Position detection and route correction of electric vehicles by dynamic wireless charging," *Ferroelectrics*, vol. 563, no. 1, pp. 103–117, Jul. 2020.
[26] Y. Yao and L. Du, "Design of intelligent vehicle based on dynamic wireless charging," in *Proc. 12th Int. Conf. Adv. Comput. Intell. (ICACI)*, Dali, China, Aug. 2020, pp. 402–407.
[27] S. Lukic and Z. Pantic, "Cutting the cord: Static and dynamic inductive wireless charging of electric vehicles," *IEEE Electrific. Mag.*, vol. 1, no. 1, pp. 57–64, Sep. 2013.

Ivan Cortes received the B.S. and M.S. degrees in mechanical engineering from Texas A&M University (TAMU), College Station, TX, USA, in 2015 and 2017, respectively, where he is currently pursuing the Ph.D. degree in mechanical engineering.

He worked as a Technician with the TAMU Turbomachinery Laboratory, assisting in research of pump seal rotordynamics. His current interest is the design and control of mechatronic systems, especially for robotics and automation.

Mr. Cortes is a fellow of the NSF-funded Texas A&M University System Louis Stokes Alliance for Minority Participation (TAMUS LSAMP) Bridge to the Doctorate (BTD) Program Cohort XI.

Won-Jong Kim (Senior Member, IEEE) received the B.S. *(summa cum laude)* and M.S. degrees in control and instrumentation engineering from Seoul National University, Seoul, South Korea, in 1989 and 1991, respectively, and the Ph.D. degree in electrical engineering and computer science from the Massachusetts Institute of Technology (MIT), Cambridge, MA, USA, in 1997.

Since 2000, he has been with the Department of Mechanical Engineering, Texas A&M University (TAMU), College Station, TX, USA, where he is currently an Associate Professor and was the inaugural Holder of the Dietz Career Development Professorship II from 2007 to 2010. He holds three U.S. patents on precision positioning systems. His current research interests include the analysis, design, and real-time control of mechatronic systems, networked control systems, and nanoscale engineering and technology.

Prof. Kim is a fellow of ASME and a member of Pi Tau Sigma. He is an Editor of *International Journal of Control, Automation, and Systems*, and is or was a Technical Editor of IEEE/ASME TRANSACTIONS ON MECHATRONICS, *ASME Journal of Dynamic Systems, Measurement and Control*, and *Asian Journal of Control*.